

Generalized pseudopolar format algorithm for radar imaging with highly suboptimal aperture length

HAN KuoYe^{1,2*}, WANG YanPing¹, CHANG XiangKe^{2,3}, TAN WeiXian¹ & HONG Wen¹

¹*Science and Technology on Microwave Imaging Laboratory (MITL), Institute of Electronics, Chinese Academy of Sciences (IECAS), Beijing 100190, China;;*

²*Institute of Computational Mathematics and Scientific Engineering Computing, Chinese Academy of Sciences (ICMSEC, CAS), Beijing 100190, China;;*

³*University of Chinese Academy of Sciences (UCAS), Beijing 100190, China*

Received ; accepted

Abstract Different from conventional spaceborne or airborne synthetic aperture radar (SAR) with optimal aperture length, an imaging radar with highly suboptimal aperture length acquires the data in short bursts by a geometry spreading over a large range. A polarlike or pseudopolar format grid is introduced to sample data close to the resolution, which presents the design of a separable kernel for efficient FFT implementation. The proposed imaging algorithm formulates the reflectivity image of the target scene as an interpolation-free double image series expansion with two usual approximation-induced phase error terms being taken into account, whereby more generalized application scenarios with high frequency, large bandwidth or larger aperture length for imaging a target scene located within either the far-field or the near-field of the radar aperture are processable with high accuracy. In addition, convergence acceleration methods in computational mathematics are introduced to accelerate the convergence of the image series expansion, so as to make the algorithm more efficient. The proposed algorithm has been validated both qualitatively and quantitatively with an extensive collection of numerical simulations and field measurements of ground-based SAR (GB-SAR) data set.

Keywords pseudopolar format, ε -algorithm, convergence acceleration, suboptimal imaging, radar imaging, synthetic aperture radar (SAR)

Citation Han K Y, Wang Y P, Chang X K, et al.. Generalized pseudopolar format algorithm for radar imaging with highly suboptimal aperture length. *Sci China Inf Sci*, 2014, xx: xxxxxx(15), doi: xxxxxxxxxxxxxxxx

1 Introduction

Synthetic aperture radar (SAR) is a valuable technique in remote sensing, which can produce two-dimensional (2-D) high resolution imagery of a wide area using a small antenna and a large bandwidth [1,2]. Taking advantage of the motion of the platform, spaceborne or airborne SARs exploit the data recorded from the radar echoes of a series of radar transmissions to computationally synthesize a very large aperture. In addition, in the last decade, an increased interest has been addressed to imaging radars with

*Corresponding author (email: kuoyehan@hotmail.com)

a highly suboptimal aperture length. One such suboptimal imaging radar is the ground-based SAR (GB-SAR), which has been used for landslide monitoring, glacier monitoring, avalanche prediction, volcano front monitoring, dams monitoring and subsidence monitoring [3,4]. Other application scenarios of the suboptimal imaging concept includes forward-looking and downward-looking 2-D and 3-D imaging of small areas with a multiple-input multiple-output (MIMO) antenna array on airborne platforms [5-7].

For imaging radars with highly suboptimal aperture length, the backscatter data are acquired in short bursts by a geometry with an aperture length of a few meters over a large range spread. The aperture length is limited by the antenna position and not by the antenna size. Most full aperture imaging algorithms [2] such as range-Doppler, range migration and chirp scaling algorithms are not suitable considering the need of large oversampling along azimuth, which is computationally intensive. In [8], a far-field pseudopolar format algorithm (FPFA) is proposed. The FPFA is fast, accurate, and obtains the reflectivity image with space-invariant resolutions in a polarlike or pseudopolar grid through an interpolation-free image series expansion. However, the FPFA is only tailored for the far-field case, whereas in practice, investigating an image scene within the near-field (e.g. Fresnel field) of the radar aperture is a commonplace when a larger aperture length and a higher nominal frequency are used in order to obtain high cross-range resolution.

In this paper, generalization of pseudopolar format processing is developed for efficient production of high-quality radar imagery while reducing the harmful effects of algorithmic approximations by a geometry with highly suboptimal aperture length. We analyzed two approximation-induced phase error terms with their respective effects. By compensating the phase error terms, the more generalized algorithm is obtained that applicable in various circumstances. Moreover, we utilize the convergence acceleration methods [9] in computational mathematics as a tool to reduce the required computational load.

This paper is organized as follows. Section 2 presents the formulation of the imaging algorithm. In Section 2.1, the imaging geometry and echo signal model are introduced. In Section 2.2, image formation is formulated in a 2-D Fourier transform with phase error terms analyzed in Section 2.3. Then in Section 2.4, a double image series expansion representation of the image with phase error compensation is given. Section 3 focuses on accelerating the convergence of the image series. Section 4 provides an extensive validity results with both numerical simulations and field measurements of GB-SAR data set. This paper is concluded in Section 5.

2 Formulation of The Algorithm

2.1 Imaging Geometry and Echo Signal Model

Consider the imaging geometry shown in Fig. 1. A highly suboptimal linear array aperture with length of L (typically 1~4 m) is formed on the x axis (azimuth), either synthetically or with physical antenna array, with the center of the array representing the origin. At each array element location x_n , the radar illuminates an area with wide angular extent and large range spread. The beam centerline is on the y axis (range), and is perpendicular to the x axis. Assuming for a point target P with polar coordinate (ρ, θ) , according to the law of cosines, the instantaneous range ρ' from the radar at x_n to the target P is

$$\rho' = \sqrt{\rho^2 + x_n^2 - 2\rho x_n \cos\left(\theta + \frac{\pi}{2}\right)}. \quad (1)$$

In practice, continuous wave (CW) technique is often used to reduce the hardware complexity [10]. So we begin with the echo signal model derived for a CW radar and write the backscatter data with target scene support Ω as

$$D(f_m, x_n) = \int_{\Omega} \sigma(\rho, \theta) \exp\left(-j\frac{4\pi f_m}{c}\rho'\right) d\rho d\theta. \quad (2)$$

with uniformly sampled frequency axis f_m and azimuth spatial axis x_n defined, respectively, as

$$f_m = f_c - \frac{B}{2} + m\Delta f = f_c - \frac{B}{2} + m\frac{B}{M-1}, \quad x_n = -\frac{L}{2} + n\Delta x_n = -\frac{L}{2} + n\frac{L}{N-1}, \quad (3)$$

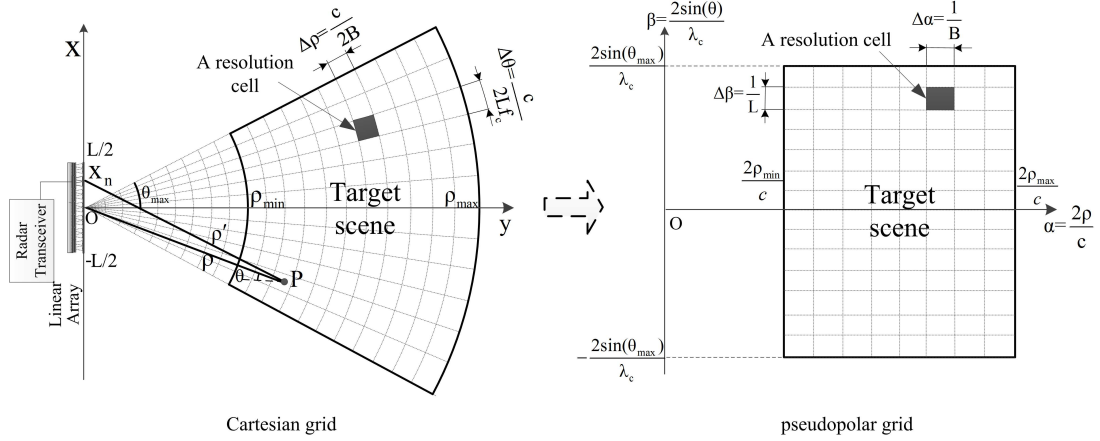


Figure 1 Geometry of an imaging radar with highly suboptimal aperture length: mapping from Cartesian grid to pseudopolar grid.

where $m = 0, 1, \dots, M-1$; $n = 0, 1, \dots, N-1$; $\sigma(\rho, \theta)$ represents the scattering coefficient or reflectivity of the target P located at polar coordinate (ρ, θ) ; c is the speed of light; f_c is the nominal center frequency; B is the total signal bandwidth; Δf is the frequency step; M is the frequency samples number; Δx_n is the synthetic or physical array element spacing; and N is the number of array elements.

The use of a fixed signal bandwidth B and a fixed aperture length L result in theoretically achievable resolutions in range and cross-range angular domain [11], respectively, as

$$\Delta\rho = \frac{c}{2B}, \quad \Delta\theta = \frac{c}{2Lf_c}. \tag{4}$$

The corresponding azimuth resolution along the x axis $\Delta x = \rho\Delta\theta/\cos(\theta)$ experiences a strong variation in the scene, according to the ratio between the far and near range, which demands for a polar gridding of the focused data to avoid huge azimuth zeropadding as is aforementioned. To deal with this problem, the image formation method formulated in the following subsection focuses the reflectivity image onto a pseudopolar format via a 2-D Fourier transform, which simplify drastically the implementation of the algorithm.

2.2 2-D Fourier Transform Representation of the Pseudopolar Formatted Image

The usual approach for focusing the backscattered data to a reflectivity image is to coherently accumulate the signal components with respect to each array element location and CW frequency [2]

$$I(\rho, \theta) = \sum_{m=0}^{M-1} \sum_{n=0}^{N-1} D(f_m, x_n) \times \exp\left(j\frac{4\pi f_m}{c}\rho'\right). \tag{5}$$

This accumulation method is accurate, but the associated computational cost is significantly large. To reduce the computation, we make near-field Fresnel approximation [12] on the range distance ρ' :

$$\rho' = \sqrt{\rho^2 + x_n^2 - 2\rho x_n \cos\left(\theta + \frac{\pi}{2}\right)} \approx \rho - \sin\theta x_n + \frac{\cos^2\theta}{2\rho} x_n^2. \tag{6}$$

A more compact approximation is the far-field Fraunhofer approximation [8,12] which keeps only the first two terms of (6) if the following assumption is satisfied:

$$\rho, \rho' \geq \frac{2L^2}{\lambda_{\min}}, \tag{7}$$

where $\lambda_{\min} = c/(f_c + B/2)$ is the smallest radar wavelength. A comparison of the phase errors introduced by the Fresnel approximation and Fraunhofer approximation is displayed in Fig. 2 when $f_c = 35$ GHz

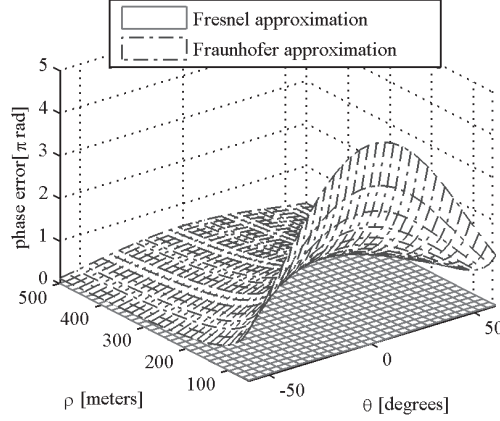


Figure 2 Phase errors introduced by Fresnel and Fraunhofer approximation.

(i.e., in the Ka-band) and $L = 4$ m. It can be seen that the Fresnel approximation is reasonably accurate, so we use it here and rewrite the image formation process (5) as

$$I(\rho, \theta) = \sum_{m=0}^{M-1} \sum_{n=0}^{N-1} D(f_m, x_n) \exp \left[j2\pi \left(f_m \frac{2\rho}{c} - x_n \frac{2\sin\theta}{\lambda_c} \right) \right] \times \exp [j\Psi_1(f_m, x_n; \theta)] \times \exp [j\Psi_2(f_m, x_n; \rho, \theta)], \quad (8)$$

where

$$\Psi_1(f_m, x_n; \theta) = -2\pi x_n \hat{f}_m \frac{2\sin\theta}{c}, \quad (9)$$

$$\Psi_2(f_m, x_n; \rho, \theta) = \frac{4\pi f_m \cos^2\theta}{c} \frac{x_n^2}{2\rho}. \quad (10)$$

with $\lambda_c = c/f_c$ representing nominal center wavelength and $\hat{f}_m = f_m - f_c$ representing baseband range frequency.

The first exponential term in (8) is the kernel of a 2D-Fourier transform with respect to (f_m, x_n) , while the remaining two exponentials $\exp[j\Psi_1]$ and $\exp[j\Psi_2]$ represent nonlinear phase error terms. In the FPPFA derivation [8], Ψ_2 is neglected based on the far-field Fraunhofer approximation of ρ' . A particular case of FPPFA also regards Ψ_1 as insignificant under the condition of having a range resolution comparable to the aperture length. In this case, the 2D-Fourier transform will produce a focused image in a polarlike or pseudopolar coordinate (α, β) , which is defined as

$$\alpha = \frac{2\rho}{c}, \quad \beta = \frac{2\sin\theta}{\lambda_c}. \quad (11)$$

The pseudopolar coordinate system resembles a polar coordinate system in that the α coordinate is directly proportional to the range coordinate ρ of the latter, while the β coordinate is proportional to the sinusoidal of the polar angle coordinate θ . In the rest of the paper, we have continued with the use of the nomenclature range and azimuth to describe the α and β coordinate of the pseudopolar formatted image. In practice, the 2D-Fourier transform is efficiently implemented via a 2-D fast Fourier transform (FFT), and the focused data locate on uniformly sampled grid as follows which is in accordance to the DFT sampling equation [13]

$$\alpha_{m'} = m' \Delta\alpha = m' \frac{1}{B} \quad (12)$$

$$\beta_{n'} = -\frac{1}{2\Delta x_n} + n' \Delta\beta = -\frac{N-1}{2L} + n' \frac{1}{L},$$

where $m' = 0, 1, \dots, M-1$; $n' = 0, 1, \dots, N-1$; $\Delta\alpha = 1/B$ and $\Delta\beta = 1/L$ represent the nominal resolution in α dimension and β dimension, respectively, both of which are space-invariant within the entire image scene.

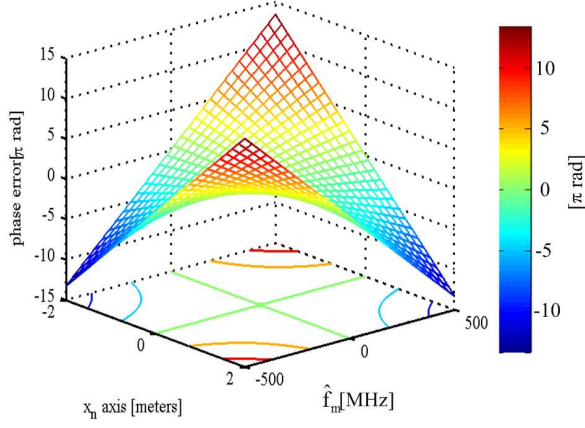


Figure 3 Phase error term Ψ_1 which manifests itself as a hyperbolic phase error.

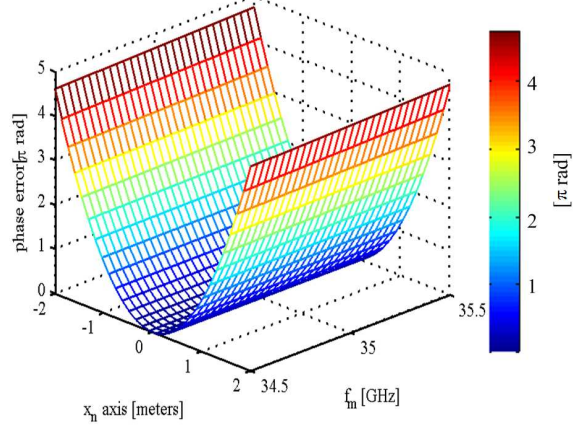


Figure 4 Phase error term Ψ_2 which manifests itself as a parabolic phase error.

2.3 Analysis of Phase Error Terms

The effect of the nonlinear phase error terms will be to convolve the ideal image with the Fourier transforms of the complex exponential terms $\exp[j\Psi_1]$ and $\exp[j\Psi_2]$, resulting the image to be defocused. When Ψ_1 and Ψ_2 are sufficiently small, the defocusing effect tends to be insignificant and a well-focused image in pseudopolar format is formed by a mere 2-D Fourier transform with respect to f_m and x_n . Conversely, the image will become heavily defocused when this condition is not met. Thus, it is imperative to examine in detail the effects of the two phase error terms, establish the limits within which an acceptable image can be produced, as well as approaches to compensate for the nonnegligible phase error terms, if any, in (8).

As can be seen from (9), Ψ_1 is an azimuth-dependent cross-product (\hat{f}_m times x_n) quadratic phase error and manifests itself as a hyperbolic phase error of the form shown in Fig. 3. This phase function results in a symmetrically defocus in both range and azimuth with severity proportional to the sinusoidal of the polar angle θ of the target. Note that Ψ_1 is range-independent and should not include blurring at $\theta = 0$. These effects are clearly seen with some examples in Section 4.

When we use the maximum values of $|\hat{f}_m|$ and $|x_n|$, which are $B/2$ and $L/2$, respectively, an upper bound of $|\Psi_1|$ is expressed as

$$|\Psi_1| = \left| 2\pi x_n \hat{f}_m \frac{2\sin\theta}{c} \right| \leq \frac{\pi\sin\theta}{2} \frac{L}{\Delta\rho}, \quad (13)$$

where $\Delta\rho = c/2B$ denotes the range resolution as in (4). Apparently, the maximum value of $|\Psi_1|$ changes linearly with the aperture length to range resolution ratio $L/\Delta\rho$, and is reached at $\theta = \pi/2$. In terms of its defocusing effect on image formation, a practical guideline is that a phase error of this type can be ignored if its peak amplitude does not exceed $\pi/2$ [14], i.e.

$$\max\{|\Psi_1|\} \leq \frac{\pi}{2}. \quad (14)$$

This happens when

$$\frac{\pi\sin\theta}{2} \frac{L}{\Delta\rho} \Big|_{\sin\theta=1} \leq \frac{\pi}{2} \Rightarrow \frac{L}{\Delta\rho} \leq 1. \quad (15)$$

Incidentally, to hold the phase error to a tolerable level of $\pi/2$, the radar aperture should have a sufficiently small dimension comparable to the range resolution. This puts a severe strain on designing the parameters of the radar system, particularly for high-resolution applications when $\Delta\rho$ is small. For example, when a system center frequency $f_c = 35$ GHz (i.e. Ka band) and bandwidth $B = 1$ GHz are used, (15) indicates a radar aperture length $L \leq 0.15$ m, which results in an azimuth resolution $\Delta x \geq 5.7$ m for targets located

at range $\rho = 200$ m, making it difficult to accommodate the azimuth resolution to the range resolution. Furthermore the situation would be worse when lower center frequency and farther range of target location are considered. In this respect, the phase error term Ψ_1 needs to be carefully compensated.

Next, let us examine the characteristics of Ψ_2 term in (10). Ψ_2 contains a cubic term $f_m x_n^2$. By rewriting f_m as $f_m = f_c(1 + \hat{f}_m/f_c)$, wherein the span of \hat{f}_m/f_c is the fractional bandwidth B/f_c of the radar system, with typical value no greater than 20% of that in conventional radar systems other than ultra-wideband radars, so that Ψ_2 is remotely dependent on the variation of f_m and most notably represents a quadratic phase error term of x_n^2 . A phase error of this form manifests itself as a parabolic phase error, as shown in Fig. 4, and is supposed to cause an azimuth defocus, the extent of which is proportional to the square of the cosine of the polar angle θ , and inversely proportional to the range coordinate ρ of target location. An upper bound of $|\Psi_2|$ is given by

$$|\Psi_2| = \left| \frac{4\pi f_m \cos^2\theta}{c} \frac{x_n^2}{2\rho} \right| \leq \frac{\pi \cos^2\theta}{2} \frac{L^2}{\rho \lambda_{\min}}, \quad (16)$$

The maximum values of $|f_m|$ and $|x_n|$ used in (16) are $f_c + B/2$ and $L/2$, respectively. Applying a criterion similar to that in (14), we will consider the defocus effect corresponding to a peak quadratic phase amplitude of $\pi/4$ or less to be negligible [14], i.e.

$$\max\{|\Psi_2|\} \leq \frac{\pi}{4}. \quad (17)$$

Inserting (16) into (17) and setting of $\theta = 0$ yields

$$\left. \frac{\pi \cos^2\theta}{2} \frac{L^2}{\rho \lambda_{\min}} \right|_{\cos\theta=1} \leq \frac{\pi}{4} \Rightarrow \rho \geq \frac{2L^2}{\lambda_{\min}}. \quad (18)$$

which is the far-field condition, in agreement with (7). In the FPFA algorithm, the assumption of (18) is made, so that the defocus effect of Ψ_2 term is neglected. However, it is quite a common scenario to have an image scene not lying within the far-field of the radar aperture when a larger radar aperture length and higher working frequency are employed. Considering a radar system with center frequency $f_c = 35$ GHz (i.e. Ka band) and bandwidth $B = 1$ GHz, a radar aperture length $L = 4$ m will give rise to a satisfactory azimuth resolution $\Delta x = 0.22$ m for boresight targets located at range $\rho = 200$ m but, nonetheless, at the cost of having a nonnegligible phase error term Ψ_2 with amplitude values shown in Fig. 4.

The imaging algorithm must cancel the phase error effects in order to maintain acceptable image quality. However, the space-variant characteristics of both Ψ_1 and Ψ_2 terms make the processing complicated. The proposed algorithm deals with this problem by expressing the target reflectivity image as an interpolation-free double series expansion and accounting for the aforementioned phase error effects in every specific order term of the image series. To facilitate the derivation, we first apply the Taylor series expansion of exponentials at origin [15] to $\exp[j\Psi_1]$ and $\exp[j\Psi_2]$ in (19) and (20), respectively, and then reformulate (8) using 2D-FFTs and image series expansion in Section 2.4.

$$\exp[j\Psi_1] = \sum_{p=0}^P \frac{1}{p!} \left[-j \frac{4\pi \sin\theta}{c} x_n \hat{f}_m \right]^p + o(|\Psi_1|^P), \quad (19)$$

$$\exp[j\Psi_2] = \sum_{q=0}^Q \frac{1}{q!} \left[j \frac{4\pi \cos^2\theta}{c} \frac{x_n^2}{2\rho} f_m \right]^q + o(|\Psi_2|^Q). \quad (20)$$

2.4 Image Series Expansion

The mapping from pseudopolar to polar coordinate is straightforward from (11), as

$$\rho = \frac{c}{2}\alpha, \quad \theta = \arcsin\left(\frac{\lambda_c}{2}\beta\right). \quad (21)$$

Inserting (19), (20) and (21) into (8), the reflectivity image of the target scene is represented as a double image series expansion of the form

$$I(\alpha_{m'}, \beta_{n'}) = \lim_{P, Q \rightarrow \infty} \sum_{p=0}^P \sum_{q=0}^Q I_{p,q}(\alpha_{m'}, \beta_{n'}), \quad (22)$$

with each specific term evaluating with an efficient 2-D FFT as

$$I_{p,q}(\alpha_{m'}, \beta_{n'}) = \frac{1}{p!} \left[j \frac{-2\pi\beta_{n'}}{f_c} \right]^p \frac{1}{q!} \left[j \frac{4\pi(1 - \frac{\lambda_c^2 \beta_{n'}^2}{4})}{c^2 \alpha_{m'}} \right]^q \times \text{FFT2D} \left[D(f_m, x_n)(x_n, \hat{f}_m)^p (x_n^2 f_m)^q \right]. \quad (23)$$

Theoretically, the double series converges to a limit of the real target reflectivity image when both P and Q approach infinite. For acceptable convergence accuracy, the partial sums of finite terms are used to evaluate the desired limit. Given the numbers of P and Q meeting the accuracy, a total number of $(P + 1) \times (Q + 1)$ terms need to be computed, each containing a 2-D FFT calculation. To further reduce the computation, we introduce convergence acceleration method, which is described in Section 3 and illustrated in Section 4.

3 Convergence Acceleration of The Image Series Expansion

3.1 Convergence Acceleration and the ε -algorithm

Convergence acceleration [9] in computational mathematics has been proved to be beneficial in accelerating the convergence of a series by eliminating the most pronounced transient behavior of the sequence of partial sums. The theory consists of seeking a transformation $T : (S_l) \rightarrow (T_l)$ to transform a slowly converging sequence (S_l) into a new sequence (T_l) converging to the same limit S faster than the initial one: $\lim_{l \rightarrow \infty} (T_l - S)/(S_l - S) = 0$. One such transformation is the Shanks transformation

$$T_l = H_{i+1}(S_l)/H_i(\Delta^2 S_l), \quad (24)$$

where $\Delta^2 S_l = S_{l+2} - 2S_{l+1} + S_l$, and H_i denotes a Hankel determinant with dimension i . For implementing the Shanks transformation, an efficient recursive method called ε -algorithm is adopted to avoid the large calculation of computing the Hankel determinant; its rules can be found in [16].

Some convergence and stability analysis for different kinds of sequences have been given in [17]. The image series representation of (23) is based on expansion of exponentials. In [17,18], the convergence analysis of the power series for the exponential function is presented, which indicates that remarkably accurate results can be obtained after a relatively small number of terms, given suitable convergence acceleration methods (e.g. ε -algorithm) are used.

3.2 Accelerating the Image Series

The conventional approach for evaluating the image series consists of computing a finite sequence of partial sums

$$S_{P,Q}(\alpha_{m'}, \beta_{n'}) = \sum_{p=0}^P \sum_{q=0}^Q I_{p,q}(\alpha_{m'}, \beta_{n'}), \quad (25)$$

where P and Q , respectively, denote the minimum order of the series over index p and q and can be determined using a similar convergence criteria as in [8].

To accelerate the convergence, the ε -algorithm is implemented point-wisely on the 2-D grid $(\alpha_{m'} \beta_{n'})$, and for each grid point, it requires a sequence of partial sums calculated from (25) as initial values, i.e. $(S_{l,Q'})_{l=0}^{P'}$ for $P' \geq Q'$, or $(S_{P',l})_{l=0}^{Q'}$ for $P' \leq Q'$, where P' and Q' denote, respectively, the minimum required order of the series over index p and q . We can estimate P' by first using a sequence of partial sums with a fixed value of Q' , e.g. $Q' = 0$. For instance, if the convergence acceleration limit of a

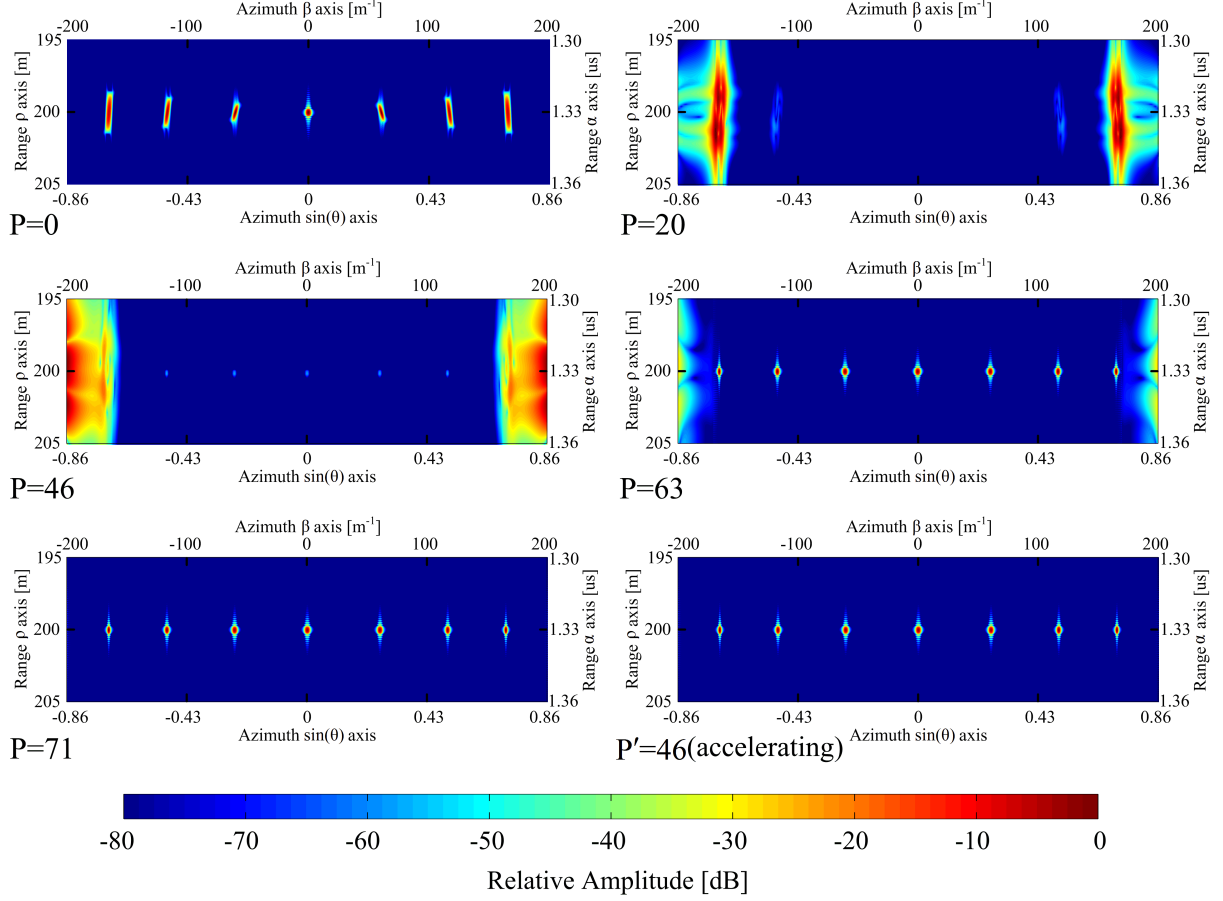


Figure 5 Reflectivity images with an increasing number of terms over the series order index p when $Q = 0$ is used.

sequence $(S_{l,0})_{l=0}^{P'}$ is represented by $S^{P'}$, then P' is determined after the following convergence condition is satisfied:

$$\frac{\sum_{k'=0}^{K-1} \sum_{m'=0}^{M-1} \sum_{n'=0}^{N-1} |S^{(P'+1)} - S^{P'}|^2}{\sum_{k'=0}^{K-1} \sum_{m'=0}^{M-1} \sum_{n'=0}^{N-1} |S^{P'}|^2} \leq 10^{-6}. \quad (26)$$

In particular, the convergence is achieved when the integrated power of the contribution from the newly added terms are much smaller than that corresponding to the image series expansion with order P' . With the same method except that the initial values are chosen such that P' is fixed, the value of Q' can also be estimated. Once P' and Q' are predetermined, the same parameters can be used in batch processing the measurement data, where a total of $(P' + 1) \times (Q' + 1)$ terms of $I_{p,q}$ in (18) need to be computed, each containing a 2-D FFT calculation. Because the implementation of ε -algorithm is computationally efficient, the overall complexity improvement after and before acceleration is roughly proportional to $[(P + 1)(Q + 1)] / [(P' + 1)(Q' + 1)]$.

4 Experimental Results

A series of numerical simulations with qualitative and quantitative analysis are used to validate the proposed method. Field measurements of GB-SAR data are also carried out to demonstrate the enhanced performance.

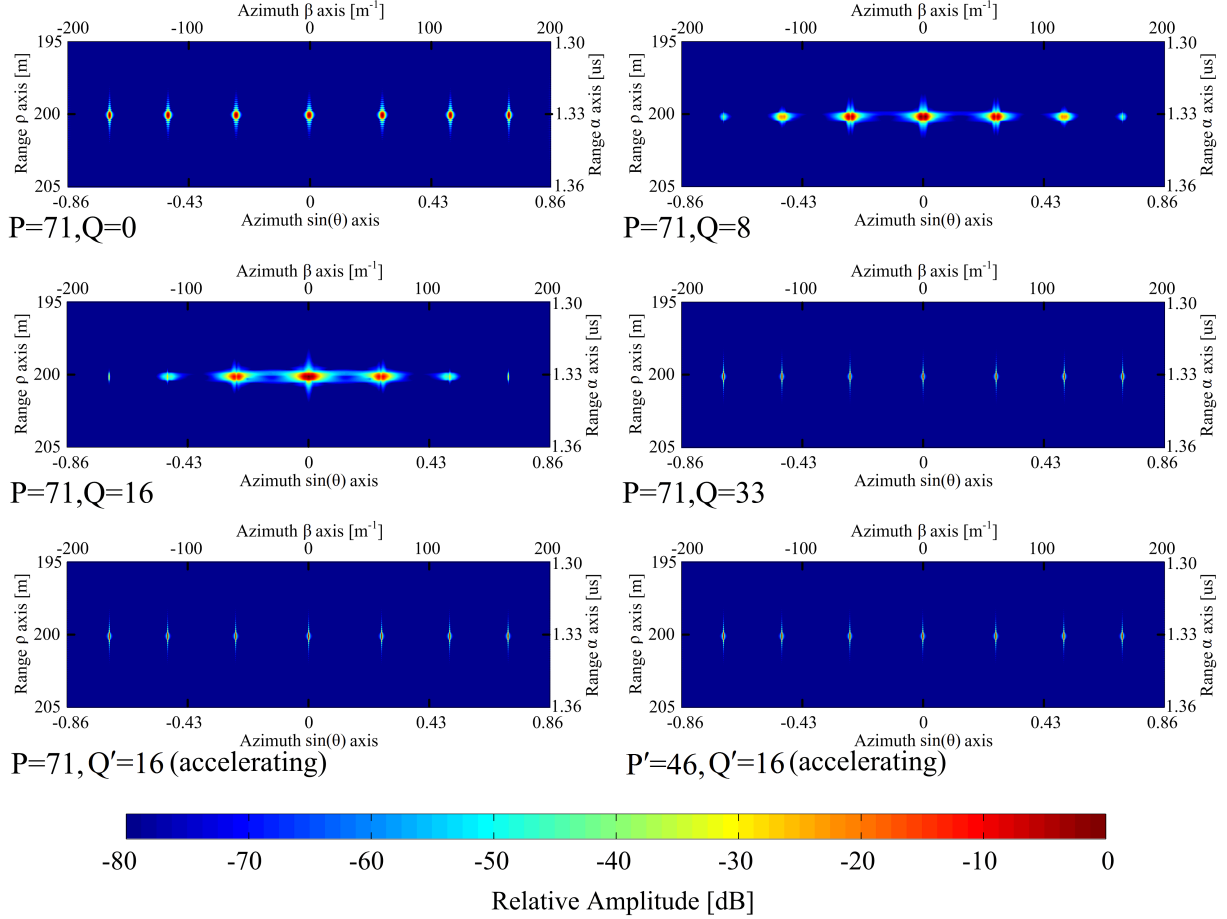


Figure 6 Reflectivity images with an increasing number over the series order index q when $P = 71$ is used and the corresponding convergence accelerating results.

4.1 Numerical Simulations

We first define an image scene consisting of seven point scatters with equal range distance of 200 m and uniformly distributed in azimuth within $-45^\circ \leq \theta \leq 45^\circ$. The radar works at a high center frequency of 35 GHz (i.e., in the Ka-band) and with a bandwidth of 1 GHz. The radar has an aperture length of 4 m long. Prior to the formation of the images, a Hanning window has been applied along the frequency f_m and the linear coordinate of the radar aperture x_n dimensions [19]. It is noted that, the ratios of $L/\Delta\rho$ and $L^2/\rho\lambda_{\min}$ are, respectively, 26.67 and 9.37, which implies the necessity of compensation of the nonnegligible phase error terms in the double series when the corresponding approximations have failed.

Fig. 5 shows the reflectivity images calculated from the partial sums of a number of terms ranging from $P = 0$ to $P = 71$, when $Q = 0$ (Fraunhofer approximation) is used, where P, Q denote the orders of the image series expansion in (25). In the zeroth order result, the center target shows only an azimuth defocus whereas targets with large off-boresight azimuth angles show astigmatism-type defocus in both range and azimuth. As the orders get increased (e.g. $P = 20, P = 46$), strong artifacts off the center of the image arise possibly because of the transient trend of the sequence of partial sums before converging. With further increase of P (e.g. $P = 63$), the artifacts gets weakened and the image series converges rapidly to a very precise reflectivity image when $P = 71$ is reached. It is important to note that with the help of convergence acceleration algorithm, a precisely good result comparable to that of $P = 71$ is obtained with the first 47 ($n = 0, 1 \dots 46$) terms of the sequence of series partial sums serving as the initial values.

Having identified the minimum required order $P = 71$ without convergence acceleration and $P' = 46$

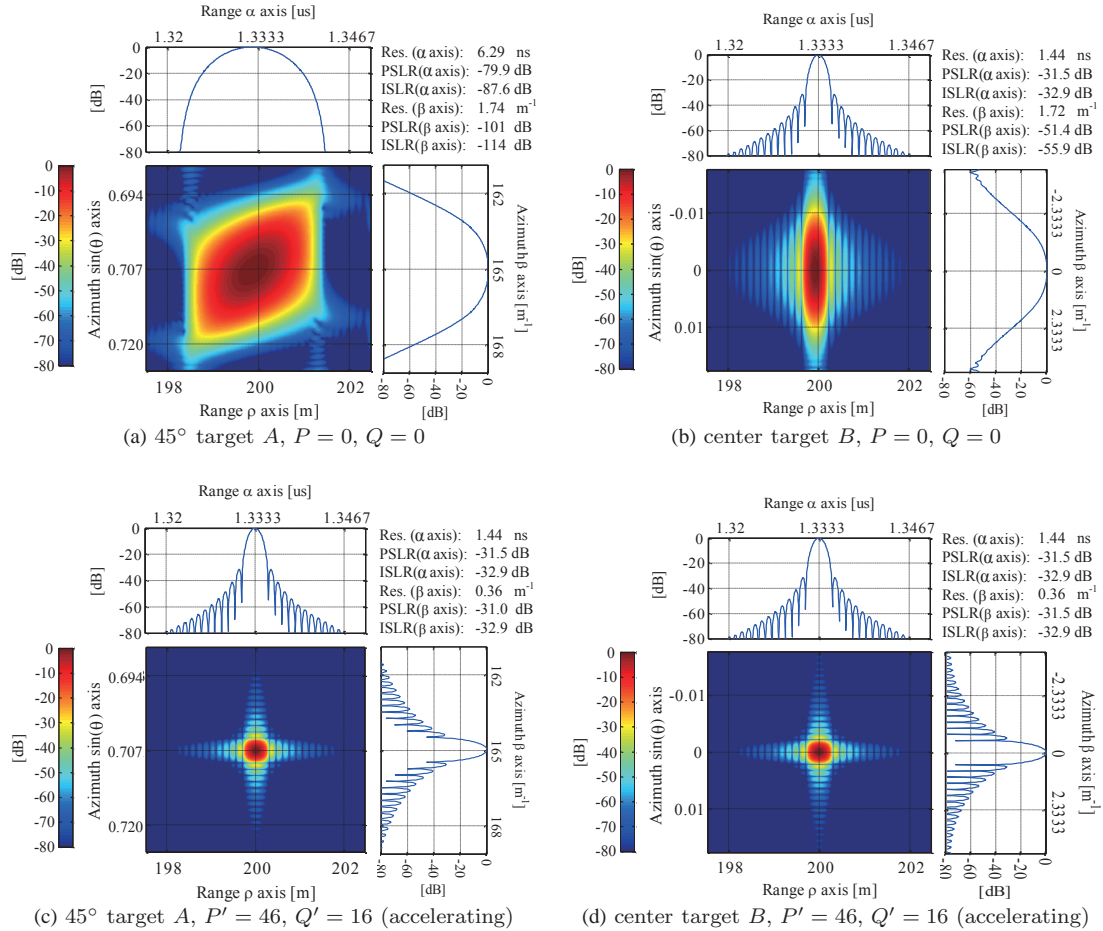


Figure 7 Point spread function (PSF) analysis of targets with off-boresight azimuth angle 45° (target A) and 0° (target B), processed by direct 2D FFT (i.e. $P = 0, Q = 0$) and convergence acceleration of image series expansion ($P' = 46, Q' = 16$).

for acceleration, we begin to investigate the other series order index q . As is clearly shown in Fig. 6, when the Ψ_1 phase error term is completely accounted for by using $P = 71$, the reflectivity images are displayed for various values of Q ranging from $Q = 0$ to $Q = 33$. The $Q = 0$ image shows the case when the far-field approximation is used which is in accordance with the result of FPFA. It can be observed that all targets show azimuth defocus and the defocus effect is most severe for the center target. By adding successive series terms, the image is blurred by artifacts (e.g. $Q = 8, Q = 16$) until the convergence is reached when $Q = 33$. That is to say, for the parameters set being investigated, the minimum order number $P = 71$ and $Q = 33$ should be used to obtain a well-focused reflectivity image. Again, we accelerate the process by convergence acceleration algorithm and estimate $Q' = 16$ to meet the accuracy level. When P' and Q' are both identified, the bigger value is used to determine the required number of initial values of ε -algorithm. In this example, a total 47 terms of a sequence of partial sums, with $Q' = 16$ fixed and $n = 0, 1 \dots 46$ stepped over the index p , result in a reflectivity image comparable to that of direct summing with $P = 71$ and $Q = 33$. The image is well focused in both range and azimuth dimensions with theoretically attainable resolutions.

A more succinct demonstration of point spread function (PSF) analysis of the center point target (target B) and the point target with off-boresight azimuth angle 45° (target A) are given in Fig. 7(a)~(d), where range and azimuth resolutions, peak sidelobe ratios (PSLR) and integrated sidelobe ratios (ISLR) are measured. Recalling (12) and considering the broadening effect of Hanning window with a factor of 1.44, the theoretical range and azimuth resolutions are $\Delta\alpha = 1.44$ ns and $\Delta\beta = 0.36$ m⁻¹. Fig. 7(a)~(b) are

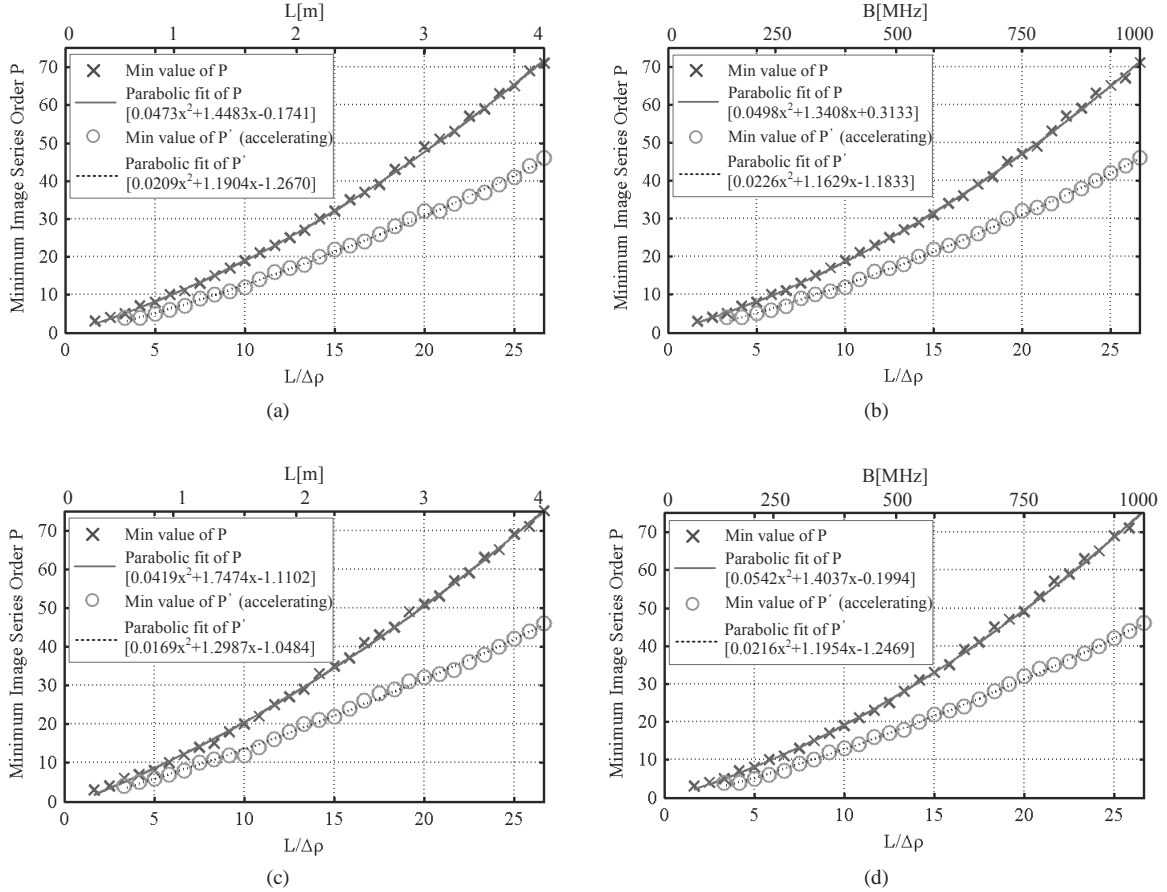


Figure 8 Minimum required order of the image series expansion over index p to guarantee the convergence with and without convergence acceleration under various parameters set, the results are expressed as a function of the aperture length to range resolution ratio ($L/\Delta\rho$). (a) Changing aperture length L and fixed frequency bandwidth ($B = 1$ GHz) when the radar works in Ka band ($f_c = 35$ GHz). (b) Changing frequency bandwidth B and fixed aperture length ($L = 4$ m) when the radar works in Ka band ($f_c = 35$ GHz). (c) Changing aperture length L and fixed frequency bandwidth ($B = 1$ GHz) when the radar works in Ku band ($f_c = 17.25$ GHz). (d) Changing frequency bandwidth B and fixed aperture length ($L = 4$ m) when the radar works in Ku band ($f_c = 17.25$ GHz).

results when direct 2D FFT is performed on the backscatter data (i.e. $P = 0$, $Q = 0$). Target A suffers from strong astigmatism-type defocus in both range and azimuth with approximately four to five fold broadening of PSF mainlobes. This defocus exists as a consequence of the combination of the two types phase error terms in Section 2.3. In both range and azimuth, the PSLR and ISLR are low because the mainlobe has absorbed most of its adjacent sidelobes. Target B is affected in azimuth only, which means the azimuth-dependent quadratic phase error term dominates the defocus effect. The range profile is perfect whereas the azimuth mainlobe is broadened several times. All these defocus effects disappear in the convergence acceleration results with $P' = 46$ and $Q' = 16$, shown in Fig. 7(c)~(d). The figures of merit being considered are in perfect agreement with theoretical values. Furthermore, all targets have identical space-invariant resolutions in the pseudopolar grid.

To complete the analysis, the minimum required orders of the image series over index p and q , namely P and Q have been estimated according to Section 3.2 under multiple parameters set. The corresponding results P' and Q' with convergence acceleration (by the ε -algorithm) are also estimated and brought to comparison. Fig. 8 expresses the result of convergence analysis over index p as a function of the aperture length to range resolution ratio ($L/\Delta\rho$) ranging from 1.67 to 26.67. Fig. 8(a)~(b) assumes the radar works at a nominal center frequency $f_c = 35$ GHz (i.e., in the Ka-band), whereas Fig. 8(c)~(d) assumes $f_c = 17.25$ GHz (i.e., in the Ku-band). In Fig. 8(a) and (c), the frequency bandwidth is fixed $B = 1$ GHz,

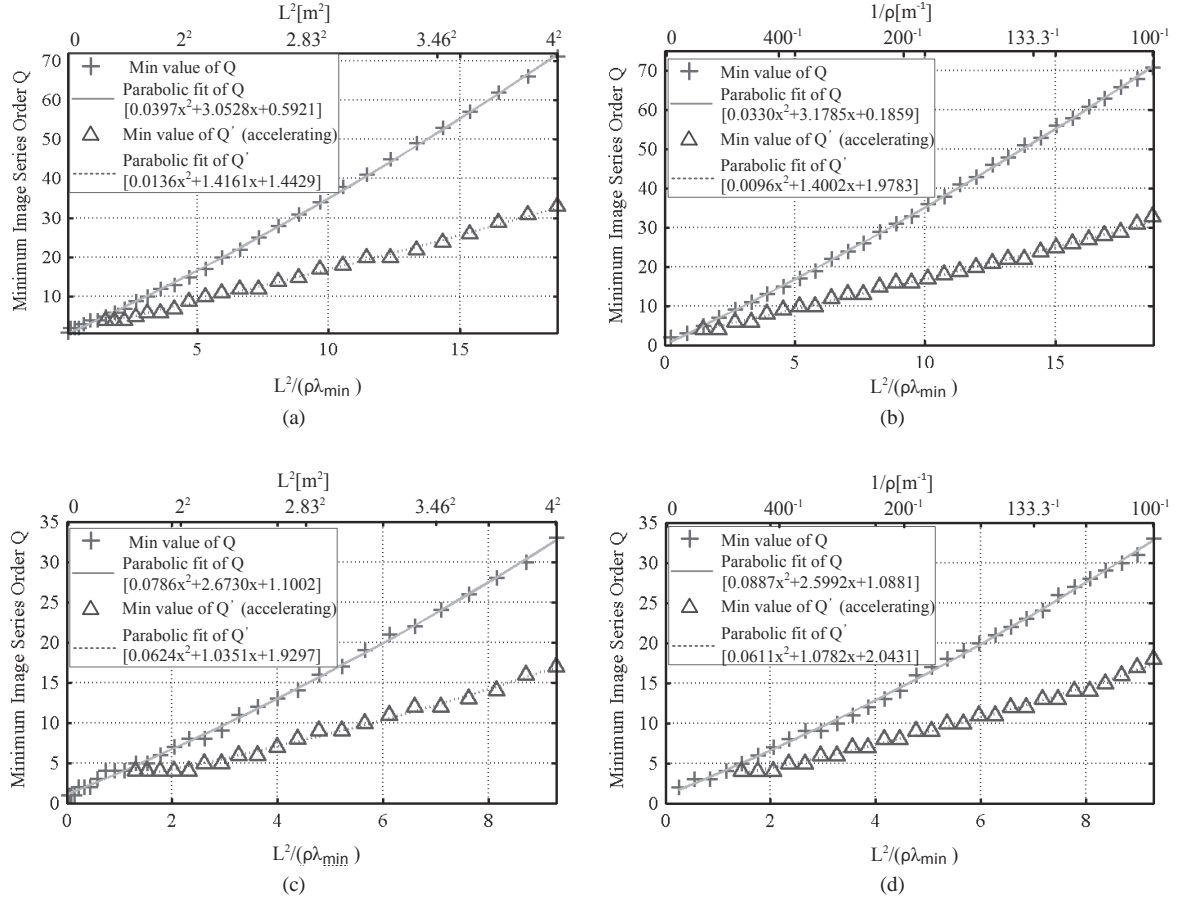


Figure 9 Minimum required order of the image series expansion over index q to guarantee the convergence with and without convergence acceleration under various parameters set, the results are expressed as a function of the ratio of squared aperture length to the product of target range and minimum wavelength ($L^2/(\rho\lambda_{\min})$). (a) Changing aperture length L and fixed target range ($\rho = 100$ m) when the radar works in Ka band ($f_c = 35$ GHz). (b) Changing target range ρ and fixed aperture length ($L = 4$ m) when the radar works in Ka band ($f_c = 35$ GHz). (c) Changing aperture length L and fixed target range ($\rho = 100$ m) when the radar works in Ku band ($f_c = 17.25$ GHz). (d) Changing target range ρ and fixed aperture length ($L = 4$ m) when the radar works in Ku band ($f_c = 17.25$ GHz).

whereas the aperture length L is changing from 0 to 4 m; in Fig. 8(b) and (d), the aperture length is fixed $L = 4$ m, whereas the frequency bandwidth B is changing from 0 to 1 GHz. In each simulation, targets located at different range distances are tested and it turns out that the results bear little relevance to the range coordinate of target location. For each plot of Fig. 8, the best parabolic fit of the estimated series order is shown. By comparison, the minimum orders of series P and P' are both smooth functions of only the ratio $L/\Delta\rho$, where the curve of P grows faster than that of P' with an increasing aperture length to range resolution ratio. When the radar works with a larger aperture length and a large bandwidth, a large number of terms in the image series expansion are supposed to be used, however, the amount of terms can be effectively cut down by convergence acceleration method. The obtained curves provide a universal lower bound to easily determine the required orders with and without convergence acceleration according to the parameter $L/\Delta\rho$.

Next, we proceed to a similar convergence analysis over index q with the simulation results shown in Fig. 9. The results are expressed as a function of the ratio of squared aperture length to the product of target range and minimum wavelength ($L^2/(\rho\lambda_{\min})$). Fig. 9(a) shows the case when the radar works at $f_c = 35$ GHz (i.e. Ka band) with a changing aperture length L (ranging from 0.25 to 4 m) to interrogate the scene targets with a fixed range distance $\rho = 100$ m. Fig. 9(b) differs from Fig. 9(a) by fixing the aperture length to $L = 4$ m and changing the targets' range coordinate from 100 to 7500 m. Fig.

9(c)~(d) set the center frequency to $f_c = 17.25$ GHz (i.e. Ku band), where in Fig. 9(c), the targets range distance is fixed $\rho = 100$ m, whereas the aperture length L is changing from 0.25 to 4 m; in Fig. 9(d), the aperture length is fixed to $L = 4$ m, whereas targets range distance is varying from 100 to 3700 m. It is deduced that the minimum orders of series Q and Q' increase rather smoothly with an increase in the ratio of $L^2/(\rho\lambda_{\min})$. Thus a large value of Q could be obtained if we design an imaging radar with larger aperture length and high frequency for high-resolution imaging of relatively nearer targets region. This value is replaced by a smaller value Q' whereby fewer terms will be used with the help of efficient convergence acceleration method. The acceleration effect is evident from Fig. 9 and likewise the curves can be regarded to be a lower bound to sensibly determine Q and Q' according to the ratio of $L^2/(\rho\lambda_{\min})$.

4.2 Field Measurements of GB-SAR data

To verify the proposed algorithm in this paper, we utilize the GB-SAR built in IECAS [20]. A VNA (Vector Network Analyzer) serves as stepped-frequency CW signal transceiver with 17.0-17.5 GHz frequency range spreading over 4001 frequency points. An HH polarization horn antenna scans-for every 0.01 m spacing-on a horizontal rail, forming a 4.6 m long synthetic aperture. The field measurement data set used for imaging verification is from a series of observations for monitoring unstable slopes around an open cast coal mine in Shanxi province, China. Fig. 10 shows the GB-SAR illuminating the observed target scene with three trihedral reflectors within it.

It is calculated that the aperture length to range resolution ratio ($L/\Delta\rho$) is 15.33, however, noting that there is a sinusoidal factor in the phase error term in (9) and that the target area is limited by the antenna beamwidth, i.e. $|\theta| \leq 15^\circ$ which is narrow, it is reasonable to expect much smaller values for P and P' . In the current experiment, P is estimated to be 14, whereas P' is estimated to be 8. Again, for image series expansion over index q , we noticed that the threshold of far-field Fraunhofer approximation is $\rho = 2469$ m, the target area being illuminated is located at the Fresnel region of the array aperture. The ratio of squared aperture length to the product of target range and minimum wavelength ($L^2/(\rho\lambda_{\min})$) ranges from 1.65 to 12.34. Accounting for sufficient convergent accuracy, the estimated minimum required number of Q and Q' are, respectively, 44 and 20, which accords with the trend line in Fig. 9.

We present the pseudopolar formatted focused image with convergence acceleration in Fig. 11. The orders $P' = 8$ and $Q' = 20$ are used, a total 21 terms of sequence of series partial sums participate in the calculation process of ε -algorithm. The three trihedral reflectors distributed between $\rho = 310$ m and $\rho = 370$ m, within azimuth angular extent $|\theta| \leq 9^\circ$ are highlighted in the image. The image obtained from FPFPA with $P = 0$ and $Q = 0$ are not shown here, nevertheless the point spread function (PSF) analyses of the three trihedral reflectors are compared with those marked in Fig. 10. Because the three trihedral reflectors are all with very small off-boresight azimuth angles, the improvement in focusing along range axis due to compensation of Ψ_1 phase error term is not distinct. Thus we only demonstrate the enhanced performance along azimuth. In Fig. 13, azimuth slices of the three trihedral reflectors are shown in dB scale. There is an obvious contrast between the mainlobe widths of PSF obtained from FPFPA and those of the algorithm we proposed. The resolution improves approximately by 3.5 times for all three reflectors until it converges to the physically attainable azimuth resolution ($\Delta\beta = 0.31 \text{ m}^{-1}$).

A noteworthy improvement in quality of focusing the image in the pseudopolar domain depends on the space-invariant range and azimuth resolutions. As a consequence, it is feasible to use the pseudopolar format at all stages of the processing chain rather than the last one, where the image is geocoded by a postfocusing regridding step. In this last step, resampling to polar or Cartesian grid is incorporated which does not need any additional calculation. Fig. 12 shows the reflectivity image of the slope area in Cartesian grid obtained by transforming the pseudopolar image via a cubic spline interpolation. This Cartesian grid lies on the data collection slant range plane, and more appropriately represents the reflectivity image when the digital elevation model (DEM) data is available.

The field measurement data is an appropriate example to test and verify the proposed algorithm. Once the minimum required orders values are estimated, huge volume data of repeated observations can be processed with the same parameters. In practical use of the method, parallel processing and hardware acceleration techniques can be a great help, the details of which are beyond the scope of this paper.

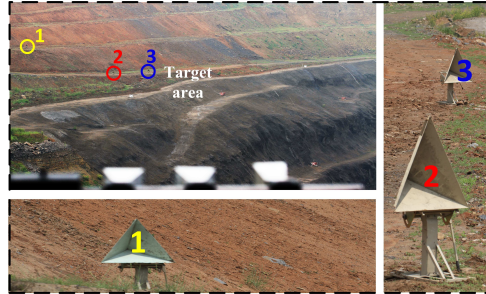


Figure 10 IECAS GB-SAR illuminating a slope area with three trihedral reflectors.

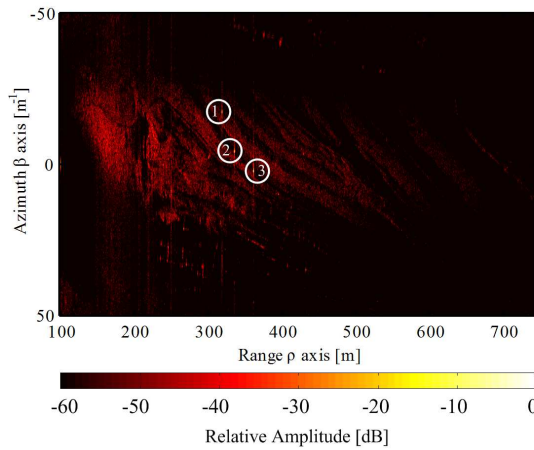


Figure 11 Real data focused with the generalized algorithm (convergence acceleration with $P' = 8$ and $Q' = 20$) in pseudopolar grid, the three trihedral reflectors are highlighted.

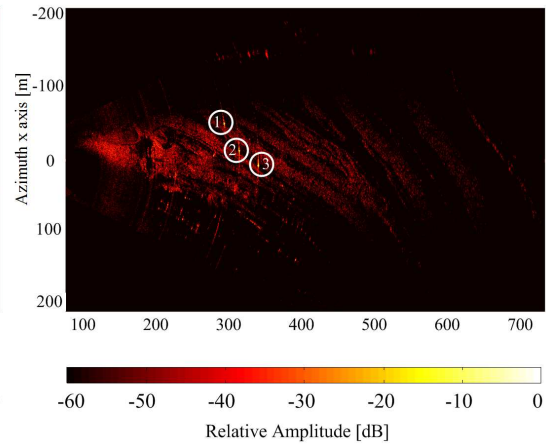
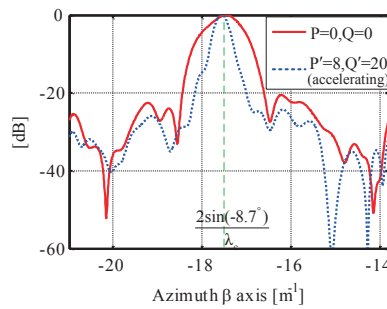
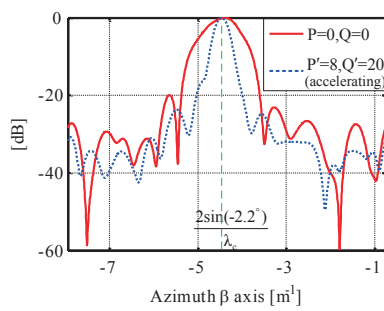


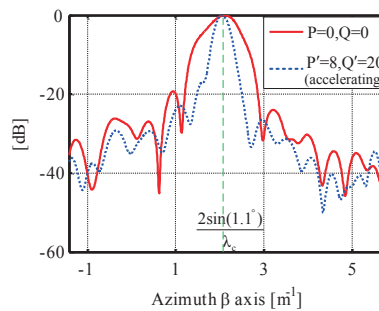
Figure 12 Reflectivity image in Cartesian grid by cubic spline interpolating the pseudopolar domain image.



(a) Trihedral reflector 1



(b) Trihedral reflector 2



(c) Trihedral reflector 3

Figure 13 Azimuth slices of the three trihedral reflectors in the pseudopolar focused image, shown in dB scale.

5 Conclusions

The main work of this paper is in examining the degradations due to algorithmic approximations and thus, developing a generalized approach to improve image focusing for imaging radars with highly suboptimal aperture lengths. The proposed algorithm extends the utility of pseudopolar format processing for application scenarios with high frequency, large bandwidth, larger aperture length and target scenes lying within either the far-field or the near-field region of the radar aperture. The algorithm is suitable for CW radars with synthetic or physical linear antenna array aperture. A series of numerical simulations and field measurements of GB-SAR data are used to validate the analysis and to demonstrate the enhanced performance of the proposed method.

Acknowledgements

The authors would like to thank the financial support by the National Natural Science Foundation of China General Program (Grant No. 61072112).

References

- 1 Curlander J C, McDonough, R N. Synthetic aperture radar: systems and signal processing. New York: Wiley, 1991.
- 2 Soumekh M. Synthetic aperture radar signal processing with Matlab algorithms. New York: Wiley, 1999.
- 3 Jungner A. Ground-based synthetic aperture radar data processing for deformation measurement. Dissertation for the Master Degree. Sweden: Royal Institute of Technology, 2009.
- 4 Tarchi D, Oliveri F, Sammartino F. MIMO Radar and Ground-Based SAR Imaging Systems: Equivalent Approaches for Remote Sensing. *IEEE Trans Geosci Remote Sens*, 2013, 51: 425–435
- 5 Krieger G, Mittermayer, J, Wendler M and et al. SIREV- Sector Imaging Radar for Enhanced Vision. In: Proceedings of the 2nd International Symposium on Image and Signal Processing and Analysis, Pula, Italy, 2001. 377–382
- 6 Klare J, Brenner A R, Ender J H. A new airborne radar for 3D imaging-image formation using the ARTINO principle. In: the 6th European Conference on Synthetic Aperture Radar, Dresden, Germany, 2006. 1–4
- 7 Wang J, Liang X D, Ding C B, et al. An improved OFDM chirp waveform used for MIMO SAR system. *SCIENCE CHINA Information Sciences*, 2014, 57(6): 062306(9)
- 8 Fortuny J. A Fast and Accurate Far-Field Pseudopolar Format Radar Imaging Algorithm. *IEEE Trans Geosci Remote Sens*, 2009, 47: 1187–1196
- 9 Brezinski C, Zaglia M R. Extrapolation methods: theory and practice. Amsterdam: North-Holland, 1991.
- 10 Mahafza B R. Radar systems analysis and design using MATLAB. London: Chapman & Hall, 2013.
- 11 Carrara W G, Goodman R S, Majewski R M, et al. Spotlight synthetic aperture radar: signal processing algorithms. Boston: Artech House, 1995.
- 12 Balanis C A. Antenna theory: analysis and design. New York: Wiley, 2012.
- 13 Oppenheim A V, Schaffer R W, Buck J R. Discrete-Time Signal Processing. Upper Saddle River: Prentice Hall, 1999.
- 14 Jakowatz C V, Wahl D E, Eichel P H, et al. Spotlight-mode synthetic aperture radar: a signal processing approach. Norwell, MA: Kluwer Academic Publishers, 1996.
- 15 Ye Q X, Shen Y H. Practical Mathematics Handbook (in Chinese). Beijing: Science Press, 2006.
- 16 Wynn P. On a device for computing the $e_m(S_n)$ transformation *Math Tables Aids Comput*, 1956, 10: 91–96
- 17 Sidi A. Practical Extrapolation Methods: Theory and Applications. Cambridge: Cambridge University Press, 2003.
- 18 Sun J Q, Chang X K, He Y, et al. An Extended Multistep Shanks Transformation and Convergence Acceleration Algorithm with Their Convergence and Stability Analysis. *Numerische Mathematik*, 2013: 1–25
- 19 Harris F J. On the use of windows for harmonic analysis with the discrete Fourier transform. *Proceedings of the IEEE*, 1978, 66(1): 51–83
- 20 Hong W, Tan W X, Wang Y P, et al. Development and Experiments of Ground-Based SAR in IECAS for Advanced SAR Imaging Technique Validation. In: the 8th European Conference on Synthetic Aperture Radar, Aachen, Germany, 2010. 1–4